applied sciences

MDPI

Article

The Effect of External Fixator Configurations on the Dynamic Compression Load: An Experimental and Numerical Study

Ana Martins Amaro [1,*], Maria Fátima Paulino [1], Luis Manuel Roseiro [1,2] and Maria Augusta Neto [1]

1 CEMMPRE (Centre of Mechanical Engineering Materials and Processes) Department of Mechanical Engineering, University of Coimbra, 3030-788 Coimbra, Portugal; maria.paulino@dem.uc.pt (M.F.P.); lroseiro@isec.pt (L.M.R.); augusta.neto@dem.uc.pt (M.A.N.)

2 Coimbra Polytechnic-ISEC, 3030-199 Coimbra, Portugal

* Correspondence: ana.amaro@dem.uc.pt; Tel.: +352-239-790-764

Received: 11 November 2019; Accepted: 16 December 2019; Published: 18 December 2019

Featured Application: Development of a medical device, which can be applied in the free clamp and capable of correlate the displacement of the free clamp and the engine electrical power consumption, in order to evaluate the osteotomy consolidation.

Abstract: (1) Objective: External fixation systems are commonly used by surgeons to ensure stabilization and consolidation of bone fractures, especially in patients who are at high risk for systematic complications. Both rigid and elastic external fixations are important in the fracture healing process. This study aims to evaluate the behavior of the Orthofix Limb Reconstruction System (LRS)® in the dynamic compression mode. (2) Methods: Experimental and numerical setups were developed using a simplified model of a human tibia which consisted of a nylon bar with a diameter of 30 mm. The bone callus was included in both setups by means of a load cell-based system, which consisted of two carbon epoxy laminated composite plates with a final stiffness of 220 N/mm. The system was evaluated experimentally and numerically, considering different numbers of pins and comparing distances between the external fixator frame and the bone, achieving a good correlation between experimental and numerical results. (3) Results: The results identified and quantified the percental load transferred to the fracture and its sensibility to the distance between the external fixator and bone. Additionally, LRS locking stiffness was evaluated which resulted from the clamp-rail clearances. The results show that the blocking effects of the free clamp movement are directly related to the fixator configuration and are responsible for changes in the amount of load that crosses the bone callus. (4) Conclusions: From the biomechanical point of view, the results suggest that the average bending span of Schanz pins and the weights of the patients should be included into clinical studies of external fixators comparisons purpose.

Keywords: bone; Orthofix Limb Reconstruction System (LRS) external fixator; bone load transfer; finite element analysis

1. Introduction

External fixation is one method of treatment for fractures, especially for patients who are at high risk for systematic complications [1]. They are frequently applied for combat and disaster related casualties [2–4], but also to manage bone defects [5]. Since World War II, design and wearing comfort of the external fixators has been improved significantly. The main biomechanical principle of

external fixation remains almost the same, i.e., providing sufficient stability at the fracture focus [6], but nowadays it is well known that micromovements in bone callus are also important to the bone consolidation process [7–10]. Hence, the challenge for external fixation research on fracture healing is to improve the biomechanics of fracture fixation, and therefore, after good initial fixation stability, a fracture heals as fast as possible. In fact, fixator stability and stiffness are very important since they influence not only the amount of interframentary movement (IFM) and alignment at fracture focus, but also affect pin-screw loosening [1,11,12].

Although there is a great variety of external fixator devices and fixator configurations, the Orthofix Limb Reconstruction System (LRS) was developed fkor the following three main indications: bone loss with shortening; bone loss without shortening; and deformity, with and without shortening, and extreme shortening. Previous studies have recommended its use in the treatment of bone defects since it offers several advantages over others [5,13–15], such as ease of application, versatility, stronger fixation, less fixator related complications, early weight bearing and primary bony union, patients satisfaction, etc. Nevertheless, there are also reports of higher complications and less patients' satisfactions when it is used for femoral lengthening [16,17]. In fact, LRS is a telescopic device in which joints are locked in order to assure a rigid fixation or unlocked to allow load sharing, or even to carry out day-to-day lengthening or transport by the patient himself. Normally, under this condition, the external fixator is extremely loaded during the treatment and pin-tract infections, as well as pin angulation is the commonest complications.

To the best of our knowledge, data comparing the mechanical performance of this fixator at different configurations and, especially, with unlocked joint, is not available. Therefore, the aim of this work is to study the behavior of the LRS fixator and optimize the distance between the external fixator frame and the bone, as well as the number of pins used to connect the external fixator to the bone, in order to promote ideal external fixator stability and decrease healing time. A load cell-based system was developed to identify and quantify the load value that is transferred to the fracture focus, when the bone is being solicited under compression. Experimental and numerical analyses were completed and the results were compared. Good correlations between the values were obtained.

2. Materials and Methods

Sixteen nylon (8 × 2) bars, thirteen six Schanz screws (side thread pins), and one Orthofix Limb Reconstruction System (LRS)® were used for the experimental study. The nylon bars were used to represent a simplified tibia, which is possible because the material properties of nylon are quite similar to those of human bone [18,19]. The fracture was simulated by screwing Schanz pins into the two nylon bars, each time, followed by the connection of pins into the clamps of the LRS external fixator. The number of pins and their location was modified eight times, leading to eight different configurations, and, in some of these configurations, the distance between the axis of the nylon bars and of the external fixator was modified three times, considering distances of 50, 70, and 90 mm. A cell load, consisting in two carbon epoxy laminated composite beams, was developed and used to represent the callus stiffness and, simultaneously, to measure the load transferred onto the artificial fracture focus.

2.1. Experimental Measurements

The nylon bars (Nylon 6, PA6) and the Schanz pins have lengths of 200 mm and of 150 mm, respectively, whereas their diameter is 30 mm and 6 mm, correspondingly. Figure 1 shows the components of the Orthofix Limb Reconstruction System (LRS)® that were used for the fixation of the nylon bars and the Schanz pins.

The load cell was developed consisting of two carbon epoxy laminated composite plates, each with 16 layers $[0^0_4/90^0_4]_s$ and dimensions of 130 × 200 × 3 [mm^3], rigidly connected by two bolted joints and two aluminum tubes, each with a length of 12 mm, assuring a gap of 12 mm between both plates, see Figure 2. Each plate was instrumented with two strain gauges from HBM® manufacturer

(reference LY13-6/-350, Darmstadt, Germany; with one measurement grid foil in constantan, 350 Ω ± 0.3%, of nominal resistance with a gage factor of 2.085 ± 0.5% at 24 °C).

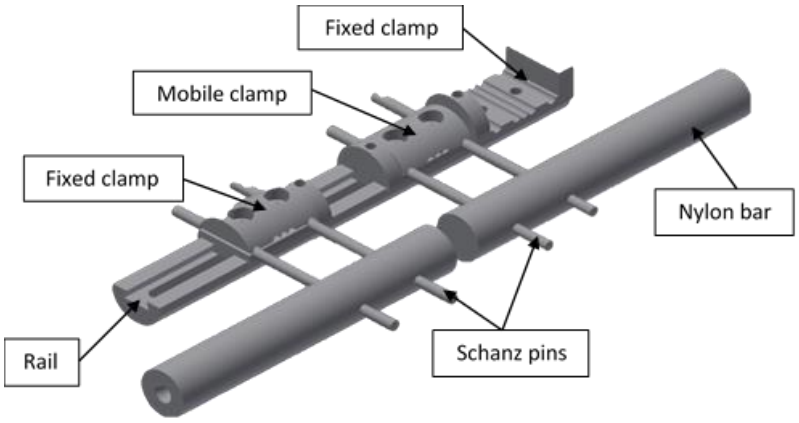

Figure 1. Three-dimensional (3D) model of the Orthofix Limb Reconstruction System (LRS) external fixator.

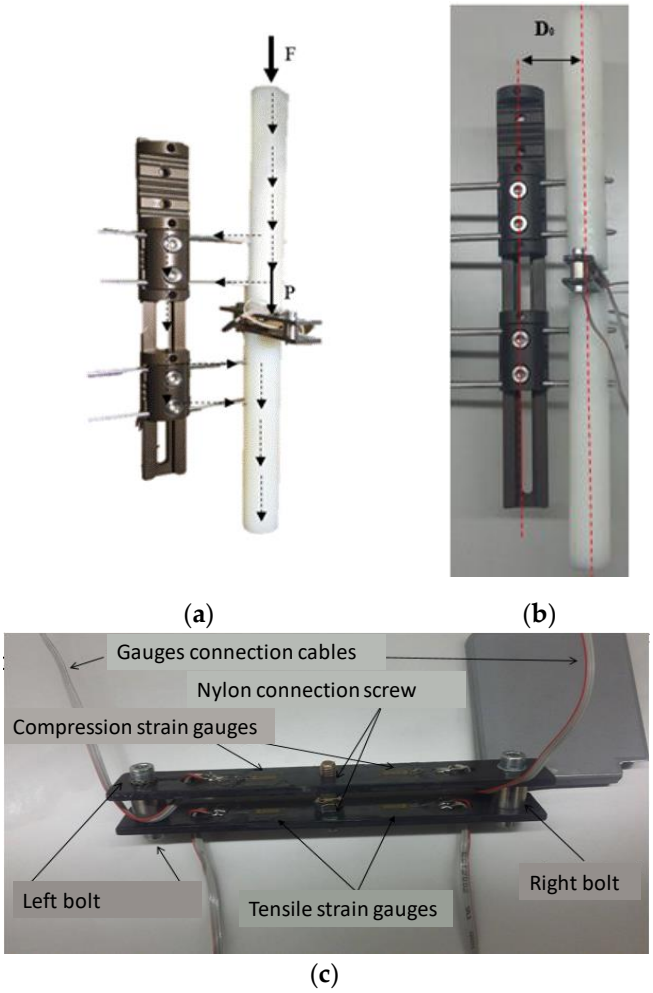

Figure 2. (**a**) Schematics distribution of loads throughout the external fixator (**b**) value of D_0, and (**c**) load cell using two laminated composite plates.

Strain gauges were glued on the longitudinal axe of one surface of the plates, at two locations with reflectional symmetry relative to the axe of the nylon bars, and a distance between them of 20 mm.

The exact position of each gauge was defined using a marking protocol. The two plates were connected by means of two bolts and two aluminum tubes, i.e., each bolt was placed inside one aluminum tube and, then, the plates were fastened to the bolts, assuring that the top surface of each plate was the instrumented surface. Later, each plate of the cell load was connected to one nylon bar by means of bolts fastened on both components, and therefore the cell load filled the gap of the fracture focus. All strain gauges were connected to a data acquisition system P3 Vishay Micro-measurements box (NI Corporation, Austin, TX, USA). The calibration and mechanical tests were performed in a universal test machine (AG-X Shimadzu®, Riverwood Drive, Columbia, MD, USA) at 1 mm/min velocity until the maximum force of 200 N was reached.

In order to evaluate and compare the amount of load transferred onto the artificial fracture focus, it was necessary to perform the assemblage of the external fixator using the Schanz pins. The distance between the axis of the external fixator and the nylon bars, which is represented in Figure 2b by D_0, was changed, considering values of 50 mm, 60 mm, 70 mm, 80 mm, 90 mm, and 100 mm. The pin positions that were considered for each axes distance are identified in Figure 3 and listed in Table 1. The distance between the fracture focus and the first pin (A) was always 20 mm, while the gap of the fracture was 18 mm.

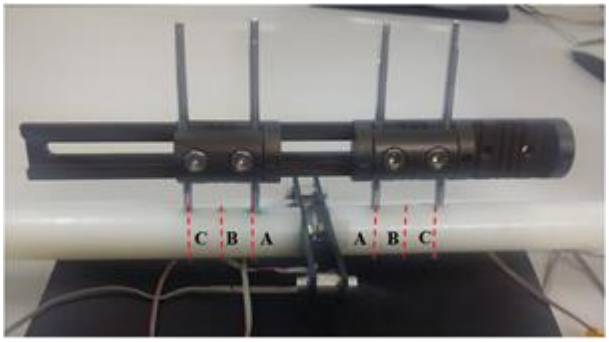

Figure 3. Identification of pin positions on the fixator configurations.

Table 1. External fixator configurations used for pin positions.

Configuration	Number of Pins in the Nylon Bars		Graphic Representation
	Upper	Bottom	
AB	2	2	
AC	2	2	
BC	2	2	
ABC	3	3	
ACAB	2	2	
BCAB	2	2	
ABCAB	3	2	
ABCAC	3	2	

The amount of load transferred to the artificial fracture focus was evaluated using a single loading direction applied to the nylon bar that was fixed to the free clamp. The load was applied using a steel sphere mounted on the cell load of the tensile machine, allowing relative rotation of the nylon bar and simulating the knee joint. The top surface of the nylon bar had a conic hole with about 1 mm of depth, avoiding the relative displacement of the sphere. The bottom surface of the nylon bar that was connected to the fixed clamp of the external fixator was supported also using a steel sphere fixed according to the standard ASTM F 1541-02 [20].

To ensure reproducibility, the nylon bars were consistently oriented on the testing platform by means of a level ruler and the forces were applied on the axis of the nylon bars. The maximum force of 200 N was held for 30 s, which created a constant time for a repeatable amount of creep to take place. Each of the eight pin configurations were tested five times and, between repetitions, the specimens were allowed to creep recovery for 10 min.

2.2. Finite Element Modeling

The loads and boundary conditions applied to all experimental pin configurations were replicated in the finite element modeling. The CAD geometry of the nylon bars were axially aligned and the CAD geometry of Schanz pins without the threads, but with the thread length included, were subtracted from the nylon bars using the Boolean operations of SolidWorks® (Dassault Systèmes SolidWorks Corporation, Waltham, MA, USA). All the LRS external fixator components were created from the measurements of each physical component and using the CAD tools available in the SolidWorks®. These CAD objects, as well as the Schanz pins, the nylon bars, and the two spheres, were posteriorly assembled considering the mean axis of the rail component as reference. The three-dimensional geometries of the two composite plates were created and connected to the nylon bars using two cylindrical bodies with 5 mm of diameter, simulating the physical bolts that were used in the experimental setup to connect the cell load to the nylon bars.

Afterwards, the finite element (FE) model of all the components was created and the three displacements (DOF) of the nodal points placed on the bottom surface of one spherical body were fixed, while the load was applied vertically to the nylon bar through another spherical body. Experimental constraints were simulated assuming contact conditions without friction between the nylon bars and the spherical bodies, and a friction coefficient of 0.75 was used to model the interface between the untightened clamp and the rail of the LRS external fixator. The bolts of the experimental setup, which were used to secure the clamps onto the LRS rail and the Schanz pins within the clamps, were simulated with material continuity. Linear elastic isotropic and transversely isotropic material properties were applied, Table 2.

Table 2. Material properties of all materials used in the finite element (FE) model.

Material Property	Carbon Epoxy	Nylon	Anodized Aluminum 7076-T6	AISI 316 L
E1 [GPA]	101.40	8.30	71.70	200
E2 [GPA]	8.40	8.30	71.70	200
E3 [GPA]	8.40	8.30	71.70	200
G12 [GPA]	5.60	3.24	26.95	79.05
G13 [GPA]	5.60	3.24	26.95	79.05
G23 [GPA]	5.60	3.24	26.95	79.05
v_{21}	0.33	0.28	0.33	0.265
v_{31}	0.33	0.28	0.33	0.265
v_{32}	0.46	0.28	0.33	0.265

The geometry of the numerical model was created in accordance with the geometry of the experimental setup and, afterwards, all the components, except the composite plates, were meshed with 8-noded unstructured regular hexahedral elements, with the incompatible modes effect included as additional degrees of freedom, and using an average element length ranging from 1 mm to 3 mm [21,22]. The accuracy of this numerical model was verified previously by a mesh convergence study and by a comparison with the numerical solution obtained with 10-noded tetrahedral finite elements [23]. The composite plates were meshed with 20-noded regular hexahedral elements using an average element length of 1 mm and connected to the nylon bars, assuming material continuity with the cylindrical bodies. Nevertheless, the interfaces between the plates and the nylon bars were modeled without friction coefficient. Moreover, in the post-processing phase, these contact surfaces were selected to evaluate the average value of the force that passes through the callus. The two composite plates were

connected using rigid links type constraints, which are available in the ADINA® [24] program. The complete finite element mesh was built with 263,651 nodes (degrees of freedom 263,651 × 3 = 790,953) and 267,780 elements, using the rule-based (mapped) meshing algorithm with preferred hexahedral (brick) cell shapes, which is available in ADINA software, and simulations were also obtained using the ADINA standard solver.

2.3. Validation Procedure

The validation of all geometrical and numerical parameters used in the FE model involved the numerical and experimental comparison of the load passing the artificial callus. Nevertheless, because the cell load is composed by two composite plates connected by two aluminum tubes, the final stiffness of the tension/compression cell load was verified using a calibration procedure as defined in the ASTM E74 Standard, leading to a stiffness of 220 N/mm. This value was obtained by performing a linear regression of the experimental force-displacement results with the coefficient of determination of 0.9587. Moreover, the load applied over the nylon bars was correlated with the strain gage measurements, by means of tensile and compression tests, and the calibrated equation was defined as,

$$\mathrm{P} = \frac{\varepsilon - 1.3718}{8.1263}, \tag{1}$$

where ε is the deformation value, in micro strains ($\mu\varepsilon$), and P is the value of load. Equation (1) was used to evaluate the value of load in the artificial fracture focus.

The experimental results show that the free clamp does not have totally free movement in the rail of the LRS external fixator. In fact, there is a bending effect in the external fixator plane that results from the deformation of the nylon bars, pins, and external fixator, which promotes the rotational movement of the free clamp actuating as a blocking force. This force appears to be dependent on the friction coefficient and on the clearance between surfaces of the clamp and rail of the LRS external fixator. Hence, the spring model, shown in Figure 4a, was proposed to obtain the locking stiffness of the fixator, where each spring represents the stiffness of the elements shown in the Figure 4b.

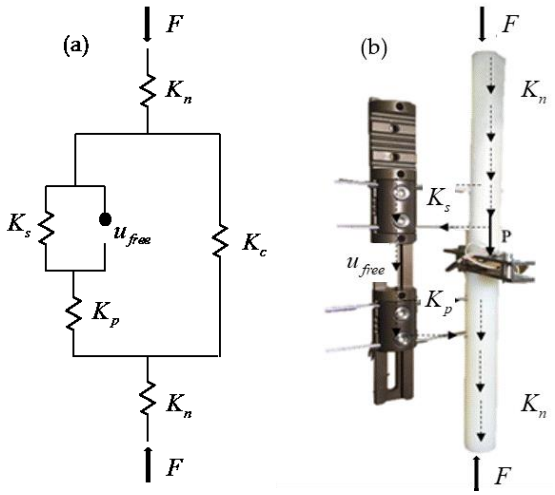

Figure 4. External fixator assembly: (**a**) spring model, where *Kn* is the nylon stiffness, Ks is the locking spring, and *Kp* is the pin stiffness; (**b**) experimental setup.

The stiffness of the pins was computed assuming that each pin was a cantilever beam which were mounted in parallel. The stiffness of the nylon was evaluated using the axial stiffness of a bar in tension/compression. The locking stiffness is computed as,

$$K_s = \frac{K_{sp}K_p}{K_p - K_{sp}};\ K_{sp} = \frac{K_{eq}K_n}{K_n - 2K_{eq}} - K_c, \tag{2}$$

where *Keq* is used to represent the experimental equivalent stiffness of fixator. Equation (2) was used to evaluate the locking stiffness of each configuration for a distance between axes of 70 mm and the results were compared with those obtained numerically. The numerical locking stiffness was evaluated using the results related to the free clamp body, the force in the cell load, as well as the total applied load. Actually, this is similar to creating the free body diagram of the free clamp, pins and nylon bar. Hence, it was computed from the ratio of the average value of the displacement of the free clamp in the compression direction to the resultant force acting on the same clamp.

3. Results

3.1. Experimental Results

Figure 5 presents the results of measurements in the AC pin positions and shows how the load in the callus varies with the applied load in one tensile/compressive test, for the callus stiffness of 220 N/mm, for each of the free pin spans. In Figure 5, 50, 70, and 90 are used to identify the distance between the axis of nylon tubes and the external fixator, and the trend lines of each measurement are also presented. In Figure 5a, all the data are approximated by one regression line and in Figure 5b the AC50 data are approximated by two different regression lines. The data obtained at the end of each tensile/compressive test is presented in Table 3, as well as the value of the interfragmentary deformation computed from the callus stiffness and the cell load (CL) value. In Table 3, TL means tensile load.

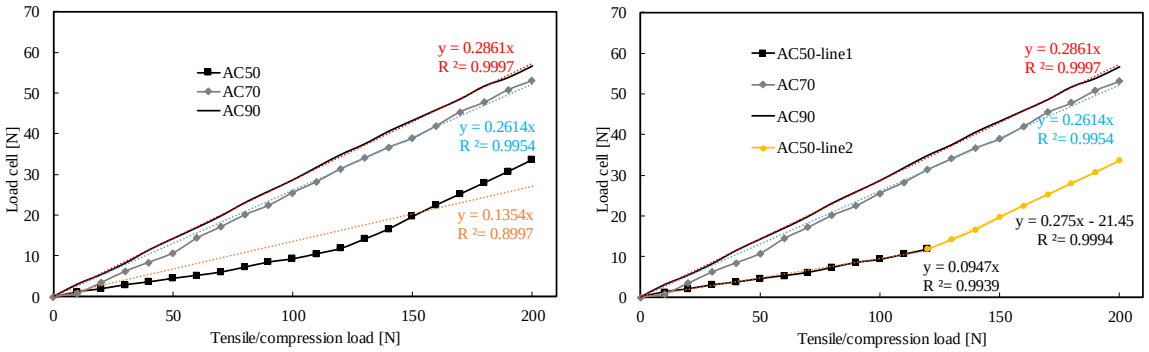

(**a**) (**b**)

Figure 5. Experimental loads in the AC configuration and three different distances between axes: (**a**) results using one regression line and (**b**) results using two regression lines for the AC50 configuration.

Table 3. Data regarding the tensile/compression tests for the AC configuration.

TL [N]	CL [N]			Interfragmentary Deformation		
	50 [mm]	70 [mm]	90 [mm]	50 [mm]	70 [mm]	90 [mm]
50	4.569	10.75	14.23	0.12%	0.27%	0.36%
100	9.368	25.58	28.63	0.24%	0.65%	0.72%
150	19.74	38.93	43.21	0.50%	0.98%	1.09%
200	33.67	53.08	56.59	0.85%	1.34%	1.43%

Some nonlinearity is observed in the CL/TL curve for the AC50 pin configuration and, because of this, the goodness-of-fit measure for this linear regression model is about 10% smaller than the R^2 of the other two regression models shown in Figure 5a. Figure 5b shows that the use of two linear regression models for the distance between axes improves the R^2 value of models' fit, but the second line shows a non-null intercept value. This observation at the origin could be associated with the discontinuity of behavior produced by the locking effect of the free clamp, which was presented in the validation section, and by the experimental adjustments that took place in the contact among spheres and nylon

bars, as well as in the contact between the free clamp and the rail of the LRS external fixator. This behavior was also observed in the other pin configurations which were tested for the same distance between axes, see Figure 6. In this figure, the goodness-of-fit measures are always higher than 0.96, i.e., the R^2 values are higher than 0.96. The slopes of the first lines of AB and AC linear regressions are similar, but the second lines of those linear regressions do not show such similar slopes. Moreover, the slope of the second line of the AC linear regression is more similar to that of the second line of the ABC linear regression, whereas the slope of the AB second linear regression is closer to the slope of the BC second linear regression.

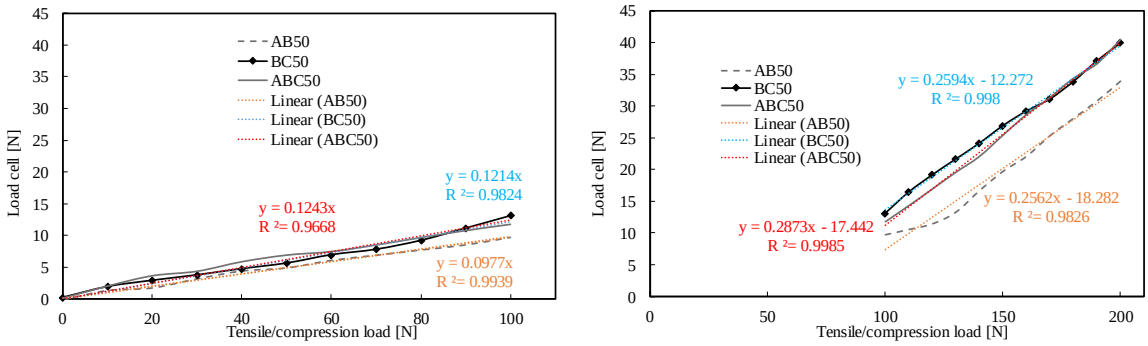

Figure 6. Experimental loads on the several pin configurations and distance between axes of 50 mm, linear regressions of the data: (**a**) in the range [0–100] N and (**b**) for the data in the range [100–200] N.

Table 4 shows all the data associated with the eight pin configurations presented in Table 1, where the ratio CL/TL represents the percentage of the total load passing through the nylon tube into the fracture focus. Some of the CL/TL ratios presented in Table 4 are quite similar to the slope of equations that are depicted in Figure 5.

Table 4. Data obtained for a compression load of 200 N and a callus stiffness of 220 Nmm^{-1}.

Configuration	50 [mm]	CL/TL	70 [mm]	CL/TL	90 [mm]	CL/TL
AB	30.66 ± 4.97	15%	52.44 ± 2.62	26%	56.85 ± 1.20	28%
AC	40.84 ± 5.69	20%	53.14 ± 0.32	27%	56.10 ± 0.66	28%
BC	36.93 ± 5.65	18%	54.79 ± 1.23	27%	57.78 ± 0.90	29%
ABC	39.24 ± 5.01	20%	52.54 ± 2.75	26%	57.39 ± 0.28	29%
ACAB	-	-	51.96 ± 3.28	26%	-	-
BCAB	-	-	54.14 ± 0.80	27%	-	-
ABCAB	-	-	50.73 ± 3.33	25%	-	-
ABCAC	-	-	54.93 ± 1.22	27%	-	-

3.2. Comparison of FEM and Experimental Results

The numerical results were only obtained for the axial distances of 70 mm and 90 mm, because these are the two distances more often used in clinical situations. The results are presented in Table 5, where the ratio CL/TL is also defined, as well as the percentage of the axial deformation in the callus.

Table 5. Numerical results for a compression load of 200 N and a callus stiffness of 220 Nmm^{-1}.

Configuration	70 [mm]			90 [mm]		
	Force [N]	Def. [%]	CL/TL	Force [N]	Def. [%]	CL/TL
AB	47.4	1.20	24%	68.31	1.73	34%
AC	46.61	1.18	23%	66.77	1.69	33%
BC	48.04	1.22	24%	68.75	1.74	34%
ABC	44.91	1.14	22%	63.9	1.62	32%
ACAB	47.12	1.20	24%	65.75	1.67	33%
BCAB	47.48	1.20	24%	70.67	1.79	35%
ABCAB	46.25	1.17	23%	67.94	1.72	34%
ABCAC	45.75	1.16	23%	66.97	1.70	33%

In order to verify the agreement between the numerical and experimental results, the AC configuration was also analysed for a distance between axes of 50 mm and the results are presented in Figure 7. The letter N is used to identify the numerical results.

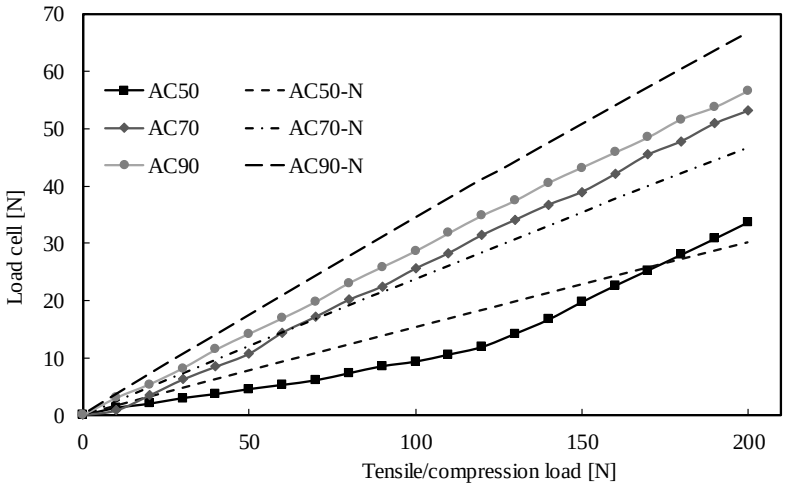

Figure 7. Experimental and numerical cell loads in the AC configuration for the three different distances between axes.

The value of the cell load in the AC50-N data and the tensile/compression load of 200 N is 30.07 N. In Figure 7, is possible to see that for the axial distances of 50 mm and 70 mm, the numerical model seems to have a stiffer behaviour than the experimental model, whereas, for the axial distance of 90 mm, it is more flexible. The predicted callus force correlated well with the experimental values, when the axial distance of 70 mm was used, and the results are reported in Figure 8.

The maximum error was of 9.18 N in the ABCAC pin configuration, which represent 16.7% of the force measured. In the symmetrical configurations the highest error was 14.5% for the ABC pin alignment. The lowest value of the predicted forces is for the ABC configuration, whereas, in the experimental tests, it was for the ABCAB configuration. This behaviour could be related to the locking stiffness of the various pin configurations that are presented in Figure 9. From the results presented in Figure 9a, for the symmetric pin configurations, it is possible to see that both numerical and experimental results show similar locking stiffness trends and the highest error was 21% for the BC pin alignment. Nevertheless, in the case of nonsymmetric pin configurations, Figure 9b, the numerical results are almost not sensitive to changes of pin configuration, whereas for the experimental results the BCAB pin alignment leads to the lowest locking stiffness. Figure 10 shows several numerical results for both AB and BC pin configurations, i.e., for the configurations with the highest and the lowest locking stiffness.

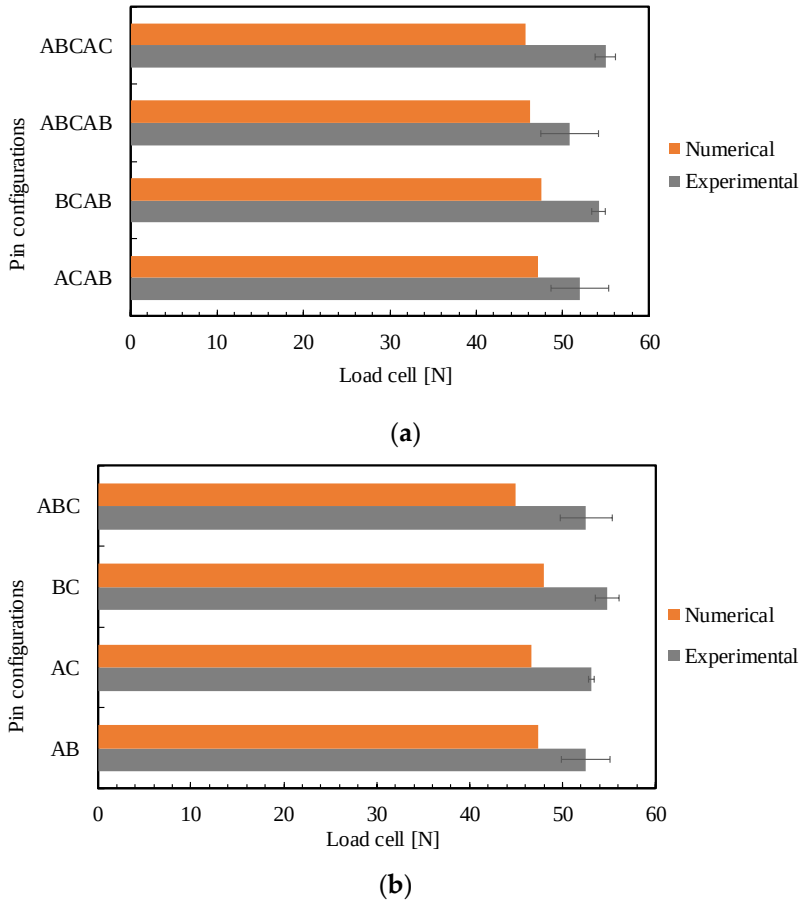

Figure 8. Predicted and measured forces in the artificial callus: (**a**) Symmetrical pin configurations and (**b**) nonsymmetrical pin configurations.

Although Figure 10 does not show significant differences among variables of the two configurations, the average y-displacement of the contact surface at the free clamps is about 1.9% smaller in the BC pin configuration than it is in the AB pin configuration, and the y-contact force is about 0.4% higher. Note that the values of y-displacement of the free clamp are not constant in the z-axe direction, which is due to the clamp rotation around the x-axe. Moreover, in the case of a free clamp rotation about its geometric center, the absolute values of y-displacement of two points geometrically positioned should be equal, but with opposite direction, leading to a null average value of the y-displacement. In the case of a non-free rotation, the tangent trigonometric function and the values of y-displacement of two points symmetrically positioned is used to estimate the rotation angle of the free clamp contact surface or even of the pins. Using this approximation, it was possible to verify that the angle of rotation of the pins and the free clamp was 1.6% higher in the BC pin alignment than in the AB configuration. Higher rotations of pins lead to higher values of contact pressure in the interface of the cell load. The distribution of the contact pressure, and the vector representation of the distributed contact pressure, on the cell load of both AB and BC pin configurations are presented in Figure 11.

The distributions of the contact pressure of both pin configurations are quite similar, but the maximum value is about 1.96% higher in the BC pin alignment. The numerical von Mises stresses were obtained at all configurations, but Table 6 contains only the results for the distance between axes of 70 mm in the upper pins and the nylon components.

Table 6. Numerical von Mises stresses in the upper pins and in the nylon components for a distance between axes of 70 mm.

Configuration	Upper Pins [MPa]			Upper-Nylon [MPa]			Bottom-Nylon [MPa]		
	A	B	C	A	B	C	A	B	C
AB	76.29	66.12	-	3.95	3.53	-	5.59	4.87	-
AC	66.68	-	70	3.75	-	3.47	5.28	-	4.92
BC	-	63.77	72.97	-	3.83	3.67	-	5.66	2.21
ABC	43.07	35.07	46.26	2.73	1.39	1.39	3.84	1.39	1.39
ACAB	69.82	-	66.48	3.74	-	3.46	5.60	4.88	-
BCAB	-	63.87	73.08	-	3.83	3.68	5.59	4.87	-
ABCAB	39.57	34.73	45.84	2.72	2.4	2.46	5.63	4.91	-
ABCAC	39.69	34.63	45.97	2.71	2.4	2.46	5.31	-	4.94

The values of Table 6 show that the ABC pin configuration leads to a more homogeneous distribution of stresses than any other pin alignments, especially in the pin holes of both nylon components. The higher level of von Mises stress in the pin A of the AB configuration seems to indicate that the locking moment in this configuration is also higher than in any other configuration.

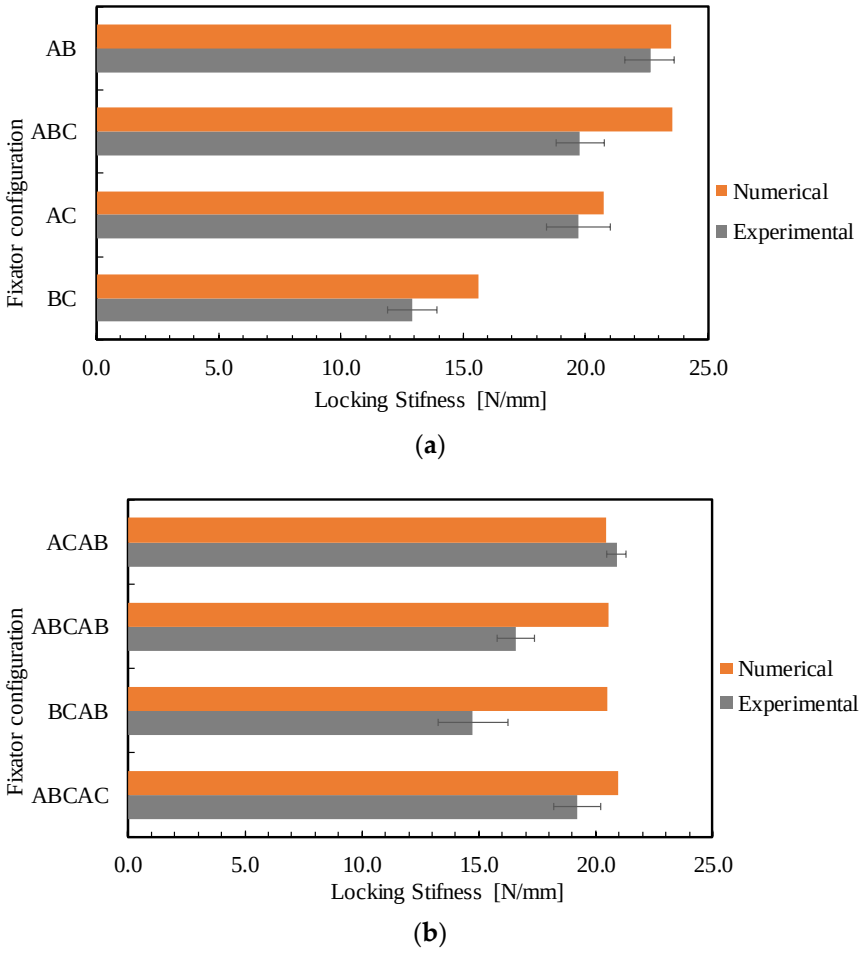

Figure 9. Predicted and measured locking stiffness: (**a**) symmetrical pin configurations; (**b**) nonsymmetrical pin configurations.

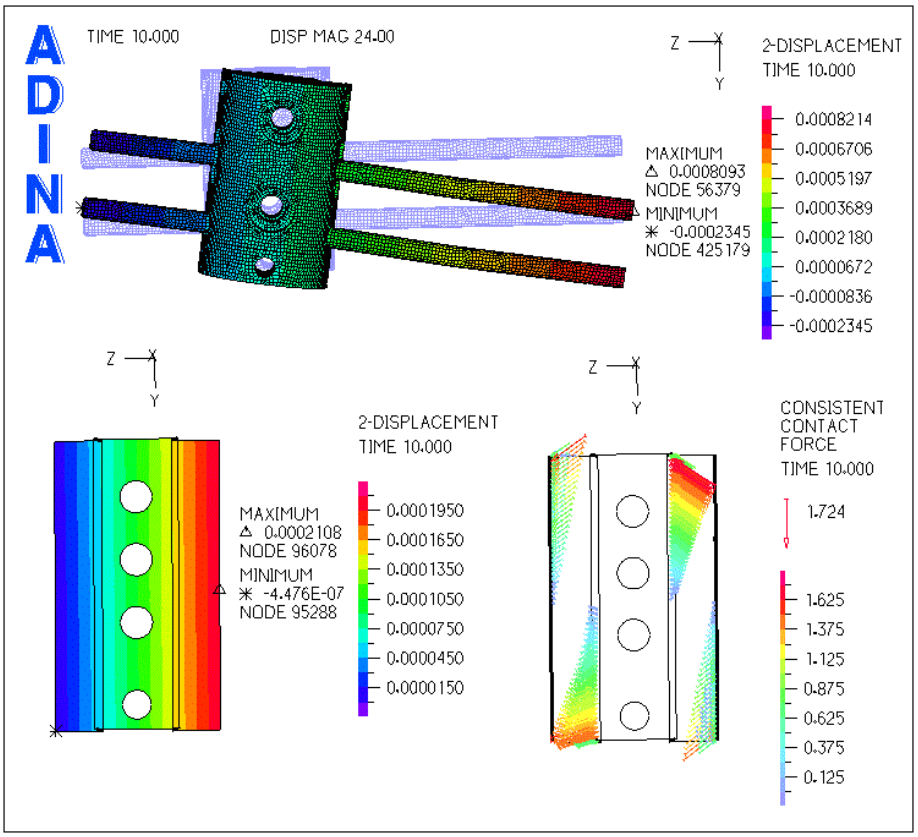

(**a**)

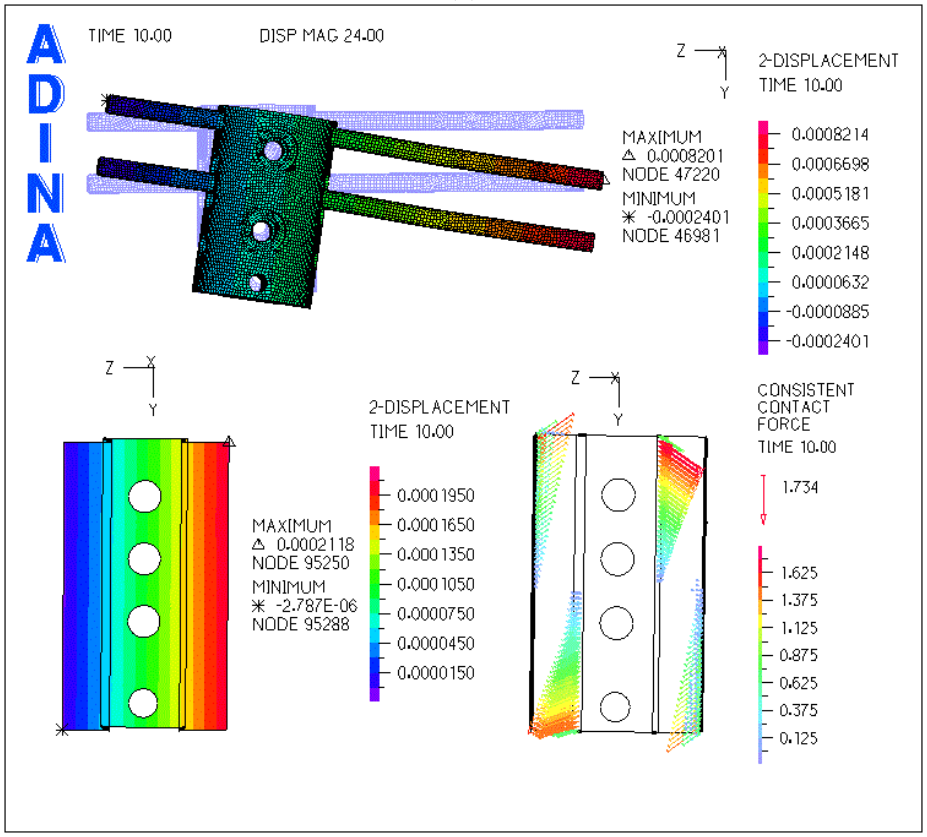

(**b**)

Figure 10. Finite element results for the pin configurations: (**a**) AB and (**b**) BC.

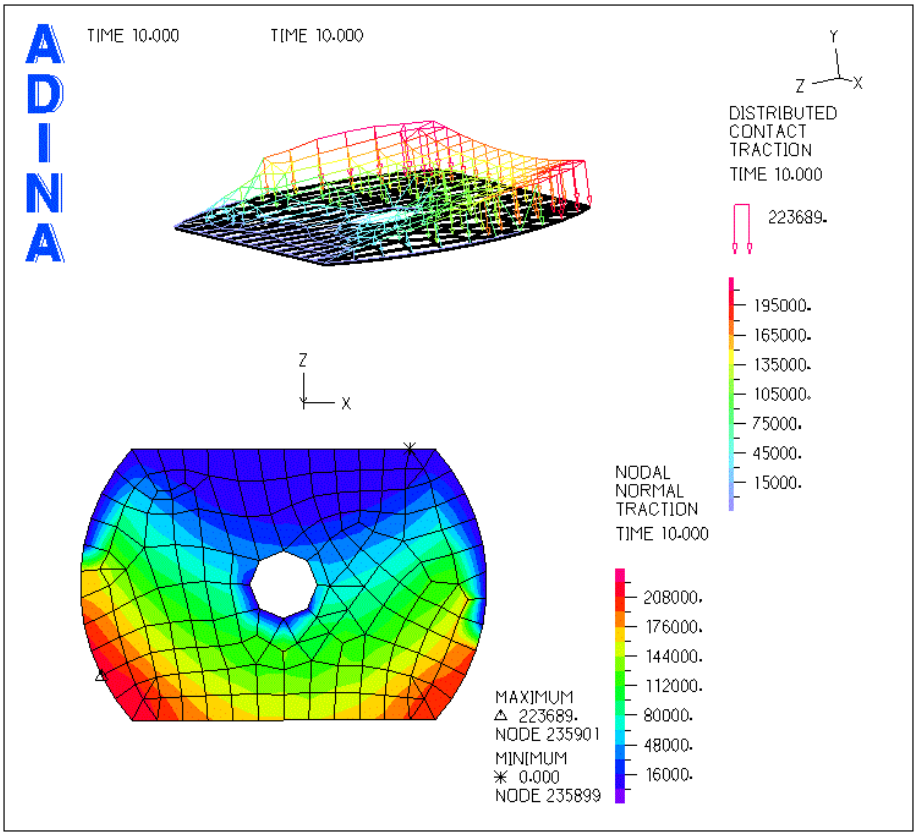

(**a**)

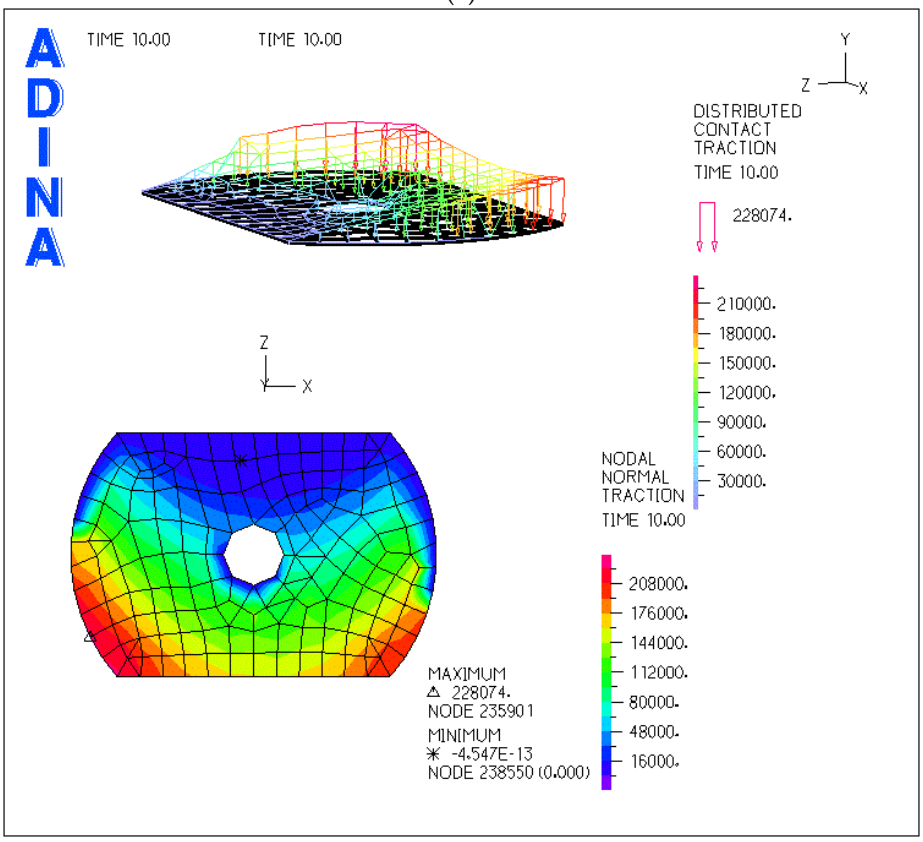

(**b**)

Figure 11. Distributed contact pressure in the cell load for the pin configurations: (**a**) AB and (**b**) BC.

4. Discussion

The aim of our study was to investigate the viability of the Orthofix Limb Reconstruction System (LRS)® in the dynamic compression mode. Although it is well accepted that the Orthofix ProCallus fixator was designed to incorporate controlled axial compression at the fracture site [1,25], the LRS external fixator it is also often used in the dynamic compression mode. Actually, the LRS fixator is especially indicated for bone correction through the techniques of bone transport, compression-distraction, partial acute shortening and transport, multifocal surgery, and bifocal lengthening [5,13,15,16]. However, for these clinical situations, patients are encouraged to perform partial weight-bearing exercises, such as walking with crutches, as early as the third or fourth day after the surgery [5,14] and, afterward, in the consolidation phase, to promote dynamic compression of the callus; releasing one of the clamps from the fixator rail, while the others remains locked, allows the LRS fixator compression mode. There are some published studies reporting comparisons of functional and clinical performance of the LRS system with other external fixators, such as Ilizarov and AO fixators [5,14,15,26]. The generality of these works concludes that the LRS fixator offers several advantages, such as ease of application, versatility, stronger fixation, less fixator related complications, early weight bearing, and early bony union. However, in their reports, researchers have not explicitly provided information of fixation strategies, such as the distance between the fixator body and the tibia axe or, even, the average value of bending span of Schanz screws, the number of pins in each bone segment, etc., thereby limiting the applicability of their results to the development of a strategy that optimizes the stress of pin-bone interfaces and the interfragmentary displacement. In fact, fracture healing by callus formation normally happens when the periosteal callus becomes stiffer, reducing interfragmentary movement while the loading amplitude is kept constant [27]. Under external fixation, the amount of interfragmentary motion is dependent not only on the fixation system, but also on other equally important factors, such as the inherent stability of fracture, the accuracy of fracture reduction, the amount of physiologic loading, and the performance of pin-bone interfaces [28]. Hence, the latest three factors were controlled in this study to investigate how the dynamic compression of the fracture site was influenced.

The experimental setup was developed using a simplified model of a human tibia, consisting of a nylon bar with 30 mm of diameter. The bone callus was included in the experimental setup by means of a load cell-based system, consisting of two carbon epoxy laminated composite plates with a final stiffness of 220 N/mm. The experimental results have shown that it was possible to quantify the load transferred to the fracture focus, during tests, and register the sensibility of the results to the distance between the external fixator and the bone.

The results of the symmetric configurations, shown in the Table 4, indicate that increasing the distance between the bone and fixator body from 50 mm to 70 mm increases the percentage of the load passing through the callus by approximately 6% to 11%. This behaviour could be justified by the global stiffness variation of the external fixator. A smaller free pin span makes the whole structure stiffer than a larger one [29,30], and for any given regenerate stiffness of callus, a more flexible fixation tends to increase the ratio of the total load supported by the callus [31,32]. Nevertheless, the results of Figure 5, and Tables 3 and 4 show also that increasing the axial distance from 70 mm to 90 mm does not change load share ratios very much. Moreover, the values of the interfragmentary deformation presented in Table 3 for the AC configuration agree with the previous conclusion. The interfragmentary strain is defined as the ratio of the relative displacement of fracture ends to the length of the initial gap. According to the interfragmentary strain hypothesis proposed by Perren [33], if the local interfragmentary strain is smaller or equal to 2% it is possible to sustain the formation of compact bone, and therefore it seems that there is no significant difference in the callus strain level between both axial distances. Nevertheless, the distance between axes of 50 mm is more sensitive to changes of the intensity of loading than the other two distances. In fact, comparisons of interfragmentary deformation among different load intensities at this axial distance, show that if the initial load is increased four times the interfragmentary deformation increases 7.4 times, whereas for the distances of 70 to 90 mm

relationships are only of 4.94 and 3.98, respectively. Moreover, the variation of the interfragmentary deformation among the three axial distances is more significant at the smallest loads than at the highest. For instance, for a load of 50 N the interfragmentary deformation for distances between axes of 70 mm and 90 mm is about 2.3 and 3.1 higher than that verified at the distance between axes of 50 mm, respectively. However, for a 200 N load the relationships are only 1.6 and 1.7 respectively. Therefore, these results show that there are at least two parameters that should be included on the external fixation comparisons purpose, the average bending span of Schanz screws and the weight of patient, i.e., the maximum load that is self-imposed. In fact, these two parameters should be accounted for, because the early weight bearing and bony union capabilities that are achieved with one external fixator are not only related to the geometric characteristics of the device (components of the fixator) or even with the psychological effect of those characteristics on patients, but also to their static or dynamic characteristics at several loads and fixator configurations (the number and spread of the pins along the bone segments, the distance between the main body of fixator and the bone) [1,25,34,35]. Nonetheless, the dynamic compression of the callus, which was induced by releasing one of the clamps from the fixator rail and the patient weight bearing, seems to be more sensitive to variations of the distance between axes of the fixator and the nylon bar than to the fixator configuration, see Table 4.

The predicted cell load values correlated well with the experimental results, especially for the axial distance of 70 mm, see Tables 4 and 5 and Figure 8. The highest errors of the load share ratio are for the ABC and ABCAC configurations, where the numerical results give values that are 14.5% and 16.7% smaller, respectively. Nevertheless, for the 90 mm axial distance, the numerical load share ratios are on average 17.4% higher than those obtained experimentally and the highest error of 20.2% was obtained for the AB configuration. Although the numerical results of the load share ratio for the 90 mm axial distance were higher than those of the 70 mm axial distance, the interfragmentary deformations increase only 0.5% on average, see Table 5. The difference between the behaviour of numerical and experimental results for the 90 mm axial distance is also visible in Figure 7, showing that the numerical model shows higher flexibility than the experimental model. This behaviour is justified by the difference of clearances between the numerical and experimental models, which influences the locking stiffness of the external fixator. In fact, from the comparison of experimental and numerical locking stiffness values for the 70 mm axial distances, as shown in Figure 9, shows that the fixator configuration has a significant effect on its experimental values. Actually, the values change from 12.92 N/mm to 22.63 N/mm, when the pin configuration changes from BC to AB, respectively. Higher values of the locking stiffness are associated with less load passing to the callus bone, due to the higher blocking effect of the free clamp, which is affected by the clearances between the free clamp and the rail body of the external fixator. Nevertheless, the y-displacement (compression displacement) of the free nylon bar depends also on the equivalent stiffness of the Schanz screws that are connected to it, hence, the cell load values are dependent on this parameter too. Combining these insights with the knowledge that the ABC pin alignment is the assemblage that is more rigid and, simultaneously, has the highest variation of the numerical and experimental locking stiffness values, it seems feasible to use this fixator configuration to make comparisons of the differences between experimental and numerical behaviour at both axial distances. For the 70 mm distance between axes, the predicted callus force was about 14.5% smaller than that measured, whereas, for the 90 mm distance between axes, it was 11.3% higher, but the numerical models of both experimental tests were created with the same number of degrees of freedom (three times the number of nodes). Hence the numerical flexibility was always the same, except the part which is inherent to the span length of the pins, and the main difference concerns the real and geometrical values of clearance between the fixator body and the clamps of the fixator.

Numerical clearance has a direct relation with the contact forces developed at contact areas and, because the numerical models have included frictional contact in the free clamp, these dry contact forces were modelled according to Coulomb's law. In this friction law, the relative tangential velocity has an important role in detecting sliding and sticking between contact surfaces. In static or quasi-static analyses the slip velocities are calculated using the nodal incremental displacements divided by the

time step [24], and therefore the time step increment has some effect on the final solution. In this study, the time step was always the same for all fixator configurations, but the automatic time stepping (ATS) method controls the time step size in order to obtain a converged solution. If there was no convergence with the specified time step, the program automatically subdivides the time step until it reaches convergence. Nevertheless, no significant time step differences were detected among the several fixator configurations. Figure 12a shows the average values of slip velocities of the two surfaces of the free clamp that contact with the two exterior surfaces of fixator rail in the ABC configuration and the distance between axes of 70 mm and 90 mm.

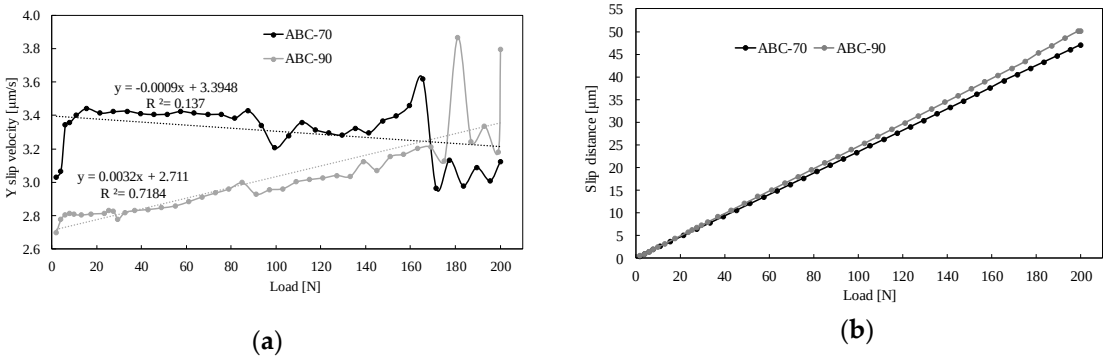

(**a**) (**b**)

Figure 12. Predicted results in the ABC-70 and ABC-90 fixator configurations: (**a**) Average slip velocity on the compression direction and (**b**) average slip distance.

The initial slip velocity predicted for the 70 mm axial distance is about 0.7 µm/s higher than that predicted for the 90 mm axial distance and, after an initial increase, it remains almost constant, but with trends to decrease, as shown by the negative slope of trendline that is depicted in the graphic. Although the trendline of the predicted slip velocity for the 90 mm axial distance shows an inverse relationship, i.e., the slope is positive, therefore, the main factor behind these differences can only be justified by the variation of span length between both fixator configurations, since the clearance is constant between numerical models. Nonetheless, from this behaviour is not possible to make a straightforward conclusion about what is the effect of fixator clearance on the force passing to the callus. Perhaps increasing the geometrical clearance between the free clamp and the fixator rail can change the slope signal of trendline of the predicted slip velocity for the 70 mm ABC fixator configuration, achieving, in this way, higher slip distance and higher callus force, as in the case of Figure 12b. Thus, improving the concordance between numerical and experimental results. But, if the increase of the same geometrical clearance would have a similar effect on the results of the 90 mm ABC fixator configuration, the force passing to the callus could get higher and, in this case, the agreement between numerical and experimental results would be lower. From this critical analysis, it is possible to confirm that fixator axial distances change the free clamp movement within the fixator rail and it is feasible that clearance could also have influence on this movement.

In addition, the contact pressure distributions predicted on the cell load, as shown in Figure 11, confirms that loads passing to the callus depend not only on the number of pins placed on the bone segment, but also from the distance between the artificial callus and first pin. In fact, it was possible to verify that decreasing this distance, i.e., changing from BC to AB pin configuration, reduces the contact pressure, but also diminishes the in-plane rotation of pins, i.e., smaller rotational misalignment, leading to a smaller misalignment of the axes of nylon bars. Moreover, the von Mises stresses presented in Table 6 show that the ABC pin configuration achieves a more homogeneous distribution of stress, which is an important factor to avoid pin site infection [36].

Even though there are differences between the numerical and experimental models, namely concerning the clearance and the continuity of connections between the free clamp and Schanz screws, and of all components connected to the locked clamp, it is worth noting that both models confirm

that the fixator configuration has a significant effect on the percentage of load passing to the callus. Moreover, disagreements between recent studies on whether mechanical stimulation is required during consolidation and remodelling healing stages [37,38] could also be related to differences between the external fixator configurations in the several studies. In fact, Claes et al. [37] performed an elastic dynamization by decreasing the stiffness of the fixation and assuming that, within the dynamization weeks, the load bearing on the operated leg does not changed considerably. In this case, the load passing to the callus was higher, and thereby increased the interfragmentary movement. On the contrary, in the work of Tufekci et al. [38] the dual unilateral fixation was maintained in all healing weeks and the dynamization was performed in the mobile fragment by a DC motor. The first main difference between these two studies is associated with the rate of change of movement in the fracture. In the first study this decrease was self-regulated by the fixation, weight bearing, and callus stiffness, while in the second study the load transmission across the bridged fracture was very limited and dynamization was controlled locally in the mobile fragment. This localized dynamization has a different impact in the remodelling process. Actually, the success of bone remodelling depends on adequate blood supply and on the gradual increase of mechanical stability [39,40], the localized modification of one condition has different effects than a global modification of both conditions. Moreover, in the physiological-like group [38], the active fixator applied 1 mm axial compressive IFMs, commencing on the fifth post-operative day, and, after three weeks, the movements were decreased in 0.25 mm increments until week six, when the applied movements were stopped [38]. This decrease of IFM does not seems related to the physiological loading on bone healing phases. If we accept that during the fracture healing process patients tend to increase weight bearing on the affected leg and that the bone callus tends to get stiffer, then it is expected that IFM should not decrease so fast [35].

In fact, one of the limitations of this work is related to the difference in IFM between the cell load and that of bone fragments, i.e., the bone callus. The IFM of bone callus is not limited to the axial displacement, there are three other movements which include: transverse, angular, and axial rotation (torsional shear) [18]. In addition, the natural weight-bearing loads include bending and shear (transverse and torsional). Actually, the natural loading is very complex and difficult to simulate. Moreover, it would require considerable resources to validate an experimental and/or numerical model that were able to predict important parameters. Nevertheless, because the generality of studies concerning the fracture healing process has been focus on the compression load [28,35,38,41,42] and the main goal of this work was to investigate the viability of the LRS fixator in the dynamic compression mode on different configurations, we were interested in relative rather than absolute results. Another limitation of this work is associated with the use of a nylon bar instead of a realistic geometry of the tibia. Nowadays, there is a great number of published works wherein realistic CAD geometries of femur and tibia have been generated using the computed tomography (CT) imaging technique [43–46]. Despite the excellent quality of these results, they are subject-specific finite element studies and, because strain variability for cadaveric specimens is larger than 100% [47], their use in test specimens concerning the external fixator configurations would require a sample of several hundred specimens. Moreover, as in any other FE model, reliable subject-specific numerical models need to ensure that modeling assumptions reflect the in vivo environment. Hence, considering the low availability of donors and the large variability of human anthropometry and material properties, it seems that synthetic bones could be an attractive alternative to this study [22]. Nevertheless, it would be interesting to develop subject-specific image-based FE models for all healing phases and try to establish a relationship between the experimental and numerical displacements of the free clamp, in order to obtain comparative results that could contribute to the evaluation of the consolidation phase and help decide when the clamp can be unlocked. Yet, these results should not be used in a quantitative way, but to compare the patient outcome between two different moments of consolidation phase. In addition, this procedure can be used on other patients and avoid exposure to additional X-ray radiation for consolidation level information.

The findings of this work cannot be applied blindly to address issues concerning the external fixation of fractured tibia, for instance the sensitivity values of load share ratios to the distance between the external fixator body and the bone. In fact, this ratio is affected not only by the distance between mentioned axes but also by the nylon stiffness, and therefore different stiffness values in real bones are expected. Nevertheless, the trends identified in this work could remain valid on real bones.

5. Conclusions

Through our study it was possible to conclude the following: (1) increasing the distance between the bone and external fixator body from 50 mm to 70 mm increases the percentage of the load passing through the callus by approximately 6% to 11%. Nevertheless, increasing this distance from 70 mm to 90 mm does not significantly change load share ratios; (2) the interfragmentary deformation at a distance between axes of 50 mm is more sensitive to changes of the intensity of loading than the other two distances; (3) the predicted cell load values correlated well with the experimental results, but the difference of the clamp-rail clearances between the numerical and experimental models had a negative influence on results agreement; (4) the clamp-rail clearances are responsible for the locking stiffness of the LRS external fixator and depending on the fixator configuration its value changes from 12.92 N/mm to 22.63 N/mm; and (5) highest values of the locking stiffness are associated with less load passing to the callus bone, due to the higher blocking effect of free clamp.

Author Contributions: M.F.P. research tests and designs, data acquisitions, finite element analysis, and manuscript revision; L.M.R. research tests and designs, data acquisitions, interpretation, and manuscript revision; A.M.A. research tests and designs, data acquisitions, interpretation, and manuscript revision; M.A.N. finite element analysis, interpretation, and manuscript writing. All authors have read and agreed to the published version of the manuscript.

Funding: This research received no external funding.

Acknowledgments: This research is sponsored by the project UID/EMS/00285/2019. The authors acknowledge the support of the students, Diana Almeida and Ricardo Silva, for having collaborated in this work.

Conflicts of Interest: The authors declare no conflict of interest.

References

1. Burgers, P.T.P.W.; Van Riel, M.P.J.M.; Vogels, L.M.M.; Stam, R.; Patka, P.; Van Lieshout, E.M.M. Rigidity of unilateral external fixators—A biomechanical study. *Injury* **2011**, *42*, 1449–1454. [CrossRef] [PubMed]
2. Lin, D.L.; Kirk, K.L.; Murphy, K.P.; McHale, K.A.; Doukas, W.C. Evaluation of orthopaedic injuries in Operation Enduring Freedom. *J. Orthop. Trauma* **2004**, *18*, 300–305. [CrossRef] [PubMed]
3. Johnson, E.N.; Burns, T.C.; Hayda, R.A.; Hospenthal, D.R.; Murray, C.K. Infectious Complications of Open Type III Tibial Fractures among Combat Casualties. *Clin. Infect. Dis.* **2007**, *45*, 409–415. [CrossRef] [PubMed]
4. Tuttle, M.S.; Smith, W.R.; Williams, A.E.; Agudelo, J.F.; Hartshorn, C.J.; Moore, E.E.; Morgan, S.J. Safety and Efficacy of Damage Control External Fixation Versus Early Definitive Stabilization for Femoral Shaft Fractures in the Multiple-Injured Patient. *J. Trauma Inj. Infect. Crit. Care* **2009**, *67*, 602–605. [CrossRef] [PubMed]
5. Yilihamu, Y.; Keremu, A.; Abulaiti, A.; Maimaiti, X.; Ren, P.; Yusufu, A. Outcomes of post-traumatic tibial osteomyelitis treated with an Orthofix LRS versus an Ilizarov external fixator. *Injury* **2017**, *48*, 1636–1643. [CrossRef]
6. Court- Brown, C. *Skeletal Trauma Basic Science, Management, and Reconstruction*, British Editioral Society of Bone and Joint Surgery, 3rd ed.; Browner Bruce, D., Jupiter Jesse, B., Levine Alan, M., Trafton Peter, G., Eds.; Saunders: Philadelphia, PA, USA, 2003; ISBN 0-7216-9175-7.
7. Sternick, M.B.; Dallacosta, D.; Bento, D.Á.; Do Reis, M.L. Relationship between rigidity of external fixator and number of pins: Computer analysis using finite elements. *Rev. Bras. Ortop.* **2012**, *47*, 646–650. [CrossRef]
8. Shahid, M.K.; Malik, S. A Review of the Biomechanical Role of a Unilateral External Fixator in the Fracture Repair Process. *EC Orthop. 3.1* **2016**, *3*, 254–260.
9. Ghiasi, M.S.; Chen, J.; Vaziri, A.; Rodriguez, E.K.; Nazarian, A. Bone fracture healing in mechanobiological modeling: A review of principles and methods. *Bone Rep.* **2017**, *6*, 87–100. [CrossRef]

10. Loi, F.; Córdova, L.A.; Pajarinen, J.; Lin, T.; Yao, Z.; Goodman, S.B. Inflammation, fracture and bone repair. *Bone* **2016**, *86*, 119–130. [CrossRef]
11. Claes, L.; Recknagel, S.; Ignatius, A. Fracture healing under healthy and inflammatory conditions. *Nat. Rev. Rheumatol.* **2012**, *8*, 133. [CrossRef]
12. Willie, B.; Adkins, K.; Zheng, X.; Simon, U.; Claes, L. Mechanical characterization of external fixator stiffness for a rat femoral fracture model. *J. Orthop. Res.* **2008**, *27*, 687–693. [CrossRef] [PubMed]
13. Hanume Gowda, S.N.; Archana, G. Treatment of infected non-union of long bones with monolateral external fixation (lrs). *J. Evol. Med. Dent. Sci.* **2014**, *3*, 14.
14. Pal, C.P.; Kumar, H.; Kumar, D.; Dinkar, K.S.; Mittal, V.; Singh, N.K. Comparative study of the results of compound tibial shaft fractures treated by Ilizarov ring fixators and limb reconstruction system fixators. *Chin. J. Traumatol.* **2015**, *18*, 347–351. [CrossRef] [PubMed]
15. Abulaiti, A.; Yilihamu, Y.; Yasheng, T.; Alike, Y.; Yusufu, A. The psychological impact of external fixation using the Ilizarov or Orthofix LRS method to treat tibial osteomyelitis with a bone defect. *Injury* **2017**, *48*, 2842–2846. [CrossRef] [PubMed]
16. Laubscher, M.; Mitchell, C.; Timms, A.; Goodier, D.; Calder, P. Outcomes following femoral lengthening. *Bone Jt. J.* **2016**, *98-B*, 1382–1388. [CrossRef]
17. Patra, S.R.; Kisan, D.; Madharia, D.; Panigrahi, N.K.; Samant, S.; Manoj, M.; Shiv, A.; Das, L.K. Management of infected non-unions of long bones using limb reconstruction system (LRS) fixator. *Int. J. Res. Orthop.* **2017**, *3*, 213. [CrossRef]
18. Gardner, T.N.; Evans, M.; Kenwright, J. The influence of external fixators on fracture motion during simulated walking. *Med. Eng. Phys.* **1996**, *18*, 305–313. [CrossRef]
19. Strebe, S.; Kim, H.; Russell, J.P.; Hsieh, A.H.; Nascone, J.; O'Toole, R.V. Analysis of strategies to increase external fixator stiffness: Is double stacking worth the cost? *Injury* **2014**, *45*, 1049–1053. [CrossRef]
20. ASTM. *Standard Specification and Test Methods for External Skeletal Fixation Devices*; ASTM F1541-01; ASTM: West Conshohocken, PA, USA, 2011.
21. Messias, A.; Neto, M.A.; Amaro, A.M.; Nicolau, P.; Roseiro, L.M. Effect of round curvature of anterior implant-supported zirconia frameworks: Finite element analysis and *in vitro* study using digital image correlation. *Comput. Methods Biomech. Biomed. Engin.* **2017**, *20*, 1236–1248. [CrossRef]
22. Lopes, V.M.M.; Neto, M.A.; Amaro, A.M.; Roseiro, L.M.; Paulino, M.F. FE and experimental study on how the cortex material properties of synthetic femurs affect strain levels. *Med. Eng. Phys.* **2017**, *46*, 96–109. [CrossRef]
23. Ramos, A.; Simões, J.A. Tetrahedral versus hexahedral finite elements in numerical modelling of the proximal femur. *Med. Eng. Phys.* **2006**, *28*, 916–924. [CrossRef] [PubMed]
24. Bathe, K. *User's Manual 2017*; ADINA R&ID: Watertown, MA, USA, 2017.
25. Chao, E.Y.; Aro, H.T.; Lewallen, D.G.; Kelly, P.J. The effect of rigidity on fracture healing in external fixation. *Clin. Orthop. Relat. Res.* **1989**, 24–35.
26. Mangukiya, H.J.; Mahajan, N.P.; Pawar, E.D.; Mane, A.; Manna, J. Functional and radiological outcome in management of compound tibia diaphyseal fracture with AO monolateral fixator versus Limb reconstruction system. *J. Orthop.* **2018**, *15*, 275–281. [CrossRef]
27. Hente, R.; Füchtmeier, B.; Schlegel, U.; Ernstberger, A.; Perren, S.M. The influence of cyclic compression and distraction on the healing of experimental tibial fractures. *J. Orthop. Res.* **2004**, *22*, 709–715. [CrossRef] [PubMed]
28. ARO, H.T.; Kelly, P.J.; Lewallen, D.G.; Chao, E.Y.S. The Effects of Physiologic Dynamic Compression on Bone Healing Under External Fixation. *Clin. Orthop. Relat. Res.* **1990**, *256*, 260–273. [CrossRef]
29. Elmedin, M.; Vahid, A.; Nedim, P.; Nedžad, R. Finite element analysis and experimental testing of stiffness of the Sarafix external fixator. *Procedia Eng.* **2015**, *100*, 1598–1607. [CrossRef]
30. Fragomen, A.T.; Rozbruch, S.R. The mechanics of external fixation. *HSS J.* **2007**, *3*, 13–29. [CrossRef]
31. Burny, F.; Burny, W.; Donkerwolcke, M.; Behrens, M. Effect of callus development on the deformation of external fixation frames. *Int. Orthop.* **2012**, *36*, 2577–2580. [CrossRef]
32. Aarnes, G.T.; Steen, H.; Ludvigsen, P.; Waanders, N.A.; Huiskes, R.; Goldstein, S.A. In vivo assessment of regenerate axial stiffness in distraction osteogenesis. *J. Orthop. Res.* **2005**, *23*, 494–498. [CrossRef]
33. Perren, S.M. Physical and biological aspects of fracture healing with special reference to internal fixation. *Clin. Orthop. Relat. Res.* **1979**, *138*, 175–196.

34. Giotakis, N.; Narayan, B. Stability with unilateral external fixation in the tibia. *Strateg. Trauma Limb Reconstr.* **2007**, *2*, 13–20. [CrossRef] [PubMed]
35. Wehner, T.; Claes, L.; Niemeyer, F.; Nolte, D.; Simon, U. Influence of the fixation stability on the healing time—A numerical study of a patient-specific fracture healing process. *Clin. Biomech.* **2010**, *25*, 606–612. [CrossRef] [PubMed]
36. Kazmers, N.H.; Fragomen, A.T.; Rozbruch, S.R. Prevention of pin site infection in external fixation: A review of the literature. *Strateg. Trauma Limb Reconstr.* **2016**, *11*, 75–85. [CrossRef] [PubMed]
37. Claes, L.; Blakytny, R.; Besse, J.; Bausewein, C.; Ignatius, A.; Willie, B. Late Dynamization by Reduced Fixation Stiffness Enhances Fracture Healing in a Rat Femoral Osteotomy Model. *J. Orthop. Trauma* **2011**, *25*, 169–174. [CrossRef] [PubMed]
38. Tufekci, P.; Tavakoli, A.; Dlaska, C.; Neumann, M.; Shanker, M.; Saifzadeh, S.; Steck, R.; Schuetz, M.; Epari, D. Early mechanical stimulation only permits timely bone healing in sheep. *J. Orthop. Res.* **2018**, *36*, 1790–1796. [CrossRef] [PubMed]
39. Marsell, R.; Einhorn, T.A. The biology of fracture healing. *Injury* **2011**, *42*, 551–555. [CrossRef]
40. Tomlinson, R.E.; Silva, M.J. Skeletal Blood Flow in Bone Repair and Maintenance. *Bone Res.* **2013**, *1*, 311–322. [CrossRef]
41. OReilly, A.; Hankenson, K.D.; Kelly, D.J. A computational model to explore the role of angiogenic impairment on endochondral ossification during fracture healing. *Biomech. Model. Mechanobiol.* **2016**, *15*, 1279–1294. [CrossRef]
42. Pietsch, M.; Niemeyer, F.; Simon, U.; Ignatius, A.; Urban, K. Modelling the fracture-healing process as a moving-interface problem using an interface-capturing approach. *Comput. Methods Biomech. Biomed. Eng.* **2018**, *21*, 512–520. [CrossRef]
43. Katz, Y.; Lubovsky, O.; Yosibash, Z. Patient-specific finite element analysis of femurs with cemented hip implants. *Clin. Biomech.* **2018**, *58*, 74–89. [CrossRef]
44. Haider, I.T.; Goldak, J.; Frei, H. Femoral fracture load and fracture pattern is accurately predicted using a gradient-enhanced quasi-brittle finite element model. *Med. Eng. Phys.* **2018**, *55*, 1–8. [CrossRef] [PubMed]
45. Falcinelli, C.; Di Martino, A.; Gizzi, A.; Vairo, G.; Denaro, V. Mechanical behavior of metastatic femurs through patient-specific computational models accounting for bone-metastasis interaction. *J. Mech. Behav. Biomed. Mater.* **2019**, *93*, 9–22. [CrossRef] [PubMed]
46. Haider, I.T.; Baggaley, M.; Brent Edwards, W. Subject-Specific Finite Element Models of the Tibia With Realistic Boundary Conditions Predict Bending Deformations Consistent With In Vivo Measurement. *J. Biomech. Eng.* **2020**, *142*, 021010. [CrossRef] [PubMed]
47. Cristofolini, L.; Viceconti, M.; Cappello, A.; Toni, A. Mechanical validation of whole bone composite femur models. *J. Biomech.* **1996**, *29*, 525–535. [CrossRef]